

Title	Luminescent optical detection of volatile electron deficient compounds by conjugated polymer nanofibers
Author(s)	Wade, Aidan; Lovera, Pierre; O'Carroll, Deirdre; Doyle, Hugh; Redmond, Gareth
Publication date	2015-03-24
Original citation	WADE, A., LOVERA, P., O'CARROLL, D., DOYLE, H. & REDMOND, G. 2015. Luminescent optical detection of volatile electron deficient compounds by conjugated polymer nanofibers. Analytical Chemistry, 87, 4421-4428. doi: 10.1021/acs.analchem.5b00309
Type of publication	Article (peer-reviewed)
Link to publisher's version	http://dx.doi.org/10.1021/acs.analchem.5b00309 Access to the full text of the published version may require a subscription.
Rights	© 2015 American Chemical Society. This document is the Accepted Manuscript version of a Published Work that appeared in final form in Analytical Chemistry (copyright © American Chemical Society) after peer review and technical editing by the publisher. To access the final edited and published work see http://dx.doi.org/10.1021/acs.analchem.5b00309
Item downloaded from	http://hdl.handle.net/10468/2457

Downloaded on 2017-02-12T10:36:58Z

Luminescent Optical Detection of Volatile Electron Deficient Compounds by Conjugated Polymer Nanofibers

Aidan Wade,[§] Pierre Lovera,[†] Deirdre O'Carroll,[‡] Hugh Doyle,^{*,†} and Gareth Redmond^{*,§}

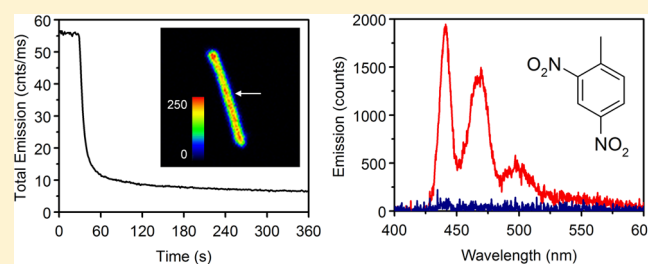
[§]School of Chemistry and Chemical Biology, University College Dublin, Belfield, Dublin 4, Ireland

[†]Tyndall National Institute, University College Cork, Lee Maltings, Cork, Ireland

[‡]Department of Materials Science and Engineering, Rutgers, The State University of New Jersey, 607 Taylor Road, Piscataway, New Jersey 08854, United States

S Supporting Information

ABSTRACT: Optical detection of volatile electron deficient analytes via fluorescence quenching is demonstrated using ca. 200 nm diameter template-synthesized polyfluorene nanofibers as nanoscale detection elements. Observed trends in analyte quenching effectiveness suggest that, in addition to energetic factors, analyte vapor pressure and polymer/analyte solubility play an important role in the emission quenching process. Individual nanofibers successfully act as luminescent reporters of volatile nitroaromatics at subparts-per-million levels. Geometric factors, relating to the nanocylindrical geometry of the fibers and to low nanofiber substrate coverage, providing a less crowded environment around fibers, appear to play a role in providing access by electron deficient quencher molecules to the excited states within the fibers, thereby facilitating the pronounced fluorescence quenching response.



Detection of trace amounts of electron deficient compounds is important for a number of applications including screening for hidden explosives, humanitarian demining, and environmental monitoring, as well as criminal and forensic investigations.^{1,2} In recent years, due to the increasing threat from terrorism and organized crime, and the consequent demand for improved security for citizens and infrastructure, much attention has focused on detection of explosives such as nitroaromatics (TNT, TNB), nitramines (RDX, HMX, Tetryl), nitrate esters (PETN, nitrocellulose), and organic peroxides (TATP, HMTD). Molecules that are not explosive themselves, but present as impurities (DNT) or tags (DMNB) in common formulations, can also be target analytes. To detect explosives with high sensitivity and high selectivity, many detection methods have been explored, including gas chromatography, mass spectroscopy, ion mobility spectroscopy and trained canine teams.²⁻⁴ However, these approaches are either bulky, expensive, or require time-consuming training and operation, limiting their deployment to fixed site screening at major transportation hubs or government buildings.⁵ Optical addressed sensors have advantages in terms of sensitivity, speed, portability, and cost-effectiveness, as well as offering a variety of transduction schemes for signal retrieval.^{1,5} Sensors for detection of explosive compounds have focused on colorimetric and fluorescence detection methods,⁶⁻⁸ with a number of sensors based on organic and inorganic conjugated polymers, small molecule fluorophores, metallo-organic complexes, and molecularly imprinted polymers reported.^{6,9-14} While each class of chemical explosives presents their own set

of challenges for detection, nitroaromatics present particular difficulties for gas phase sensors due to their low vapor pressures.¹⁵ However, these electron deficient analytes bind strongly to the electron-rich polymer thin films typically used, while the subsequent fluorescence quenching response is amplified by the molecular wire configuration of the chromophores.^{14,16,17} The Fido explosives sensing platform, based on this amplifying fluorescent polymers (AFP) approach, is capable of detecting a range of nitrated explosive vapors.^{18,19} Although most optically addressed detectors have been based on planar transducer formats such as spun cast thin films or spotted arrays, one-dimensional (1D) nanostructures such as nanowires, nanotubes, and nanofibers have been attracting increasing attention as chemical and biological sensors.²⁰⁻²⁷ Organic 1D nanostructures, possessing the processability and high photoluminescence (PL) efficiency of their constituent molecular components,²⁸⁻³⁰ also offer advantages for sensing applications including their high surface-to-volume ratios and analyte diffusion into the organic matrix, which is more difficult for inorganic semiconductor nanowires or glass nanofibers.^{31,32} The long-range exciton migration intrinsic to the well-organized molecular arrangement within these nanostructures magnifies the fluorescence quenching response to surface adsorbed analytes.^{10,17,33}

Received: January 21, 2015

Accepted: March 24, 2015

75 Current strategies employed to enhance the sensitivity of 1D
76 nanostructures for sensing applications are focused on the
77 structure-level design by controlling the structure morphol-
78 ogy.^{34,35} The structures of various 1D nanomaterials, and their
79 hierarchical assemblies including meshes and nanoarrays,
80 effectively influence the absorption and diffusion behaviors of
81 the analyte.^{18,36,37} Therefore, considerable efforts have been
82 placed on optimizing the 1D structures and assemblies to
83 achieve high sensitivity, selectivity and fast time response.³⁸
84 Besides tailoring the morphology and size of the nanostruc-
85 tures, binary and multicomponent materials have investigated
86 to achieve superior sensing performance.³⁹ Doping is
87 commonly used to achieve controlled changes to photophysical
88 characteristics and consequent enhancements of sensing
89 performance.³⁴ The composite nanostructures can not only
90 combine the properties of different compounds but also
91 generate new functionality based on intermolecular interactions
92 and energy transfers.^{40,41} In this article, we report on the
93 luminescent optical detection of volatile electron deficient
94 compounds by conjugated polymer nanofibers based on
95 poly(9,9-dioctylfluorenyl-2,7-diyl), (PFO). The performance
96 of dense arrays of luminescent PFO nanofibers for gas phase
97 detection of trace amounts of 2,4-dinitrotoluene (DNT),
98 anthraquinone (AQ), and duroquinone (DQ) analytes was
99 compared with that of a thin film based sensor format prepared
100 using the same parent material. Following this, the effect of
101 packing density on the fluorescence quenching response is
102 investigated. Finally, detection of nitroaromatics at subparts-
103 per-million levels is demonstrated on individual nanofibers by
104 scanning confocal microscopy and photoluminescence spec-
105 troscopy.

106 ■ EXPERIMENTAL METHODS

107 **Materials.** Porous alumina membranes with nominal pore
108 diameters of 200 nm were purchased from Whatman Ltd.
109 Poly(9,9-dioctylfluorenyl-2,7-diyl), PFO, with a polydispersity
110 index of 3.0 and a weight-average of 100 000 (PS standards)
111 was purchased from H.W. Sands Corp. Sulfuric acid (H₂SO₄;
112 95–98%), sodium hydroxide, anhydrous tetrahydrofuran
113 (THF), chloroform (CHCl₃), hydrochloric acid (HCl; 37%
114 in water), methanol, acetone, decane, 2,4-dinitrotoluene (2,4-
115 DNT; 97%), duroquinone (DQ; 97%), and anthraquinone
116 (AQ; 98%) were purchased from Sigma-Aldrich, Ltd. All
117 reagents and solvents were used without further purification.
118 Deionized water (>16.1 MΩ cm, Milli-Q, Millipore) was used
119 for all aqueous solutions.

120 **Preparation of Polyfluorene Nanofibers.** A concen-
121 trated solution of PFO (60 mg/mL) was prepared by dissolving
122 the polymer in anhydrous THF in a sealed amber glass vial,
123 while heating to 60 °C and stirring vigorously for 30 min. The
124 solution was allowed cool to room temperature. Alumina
125 membranes were sonicated in methanol and air-dried prior to
126 use. A 50 μL drop of polymer solution was deposited on top of
127 a membrane. A glass coverslip was placed on top of the drop,
128 facilitating penetration of the solution into the template pores.
129 A weight of ca. 2.5 kg was applied overnight. Following this,
130 excess material was removed from the template surface by
131 scraping with a razor blade. The template, with embedded
132 nanofibers, was soaked in aqueous NaOH (3 M) for 12 h to
133 dissolve the alumina host. The NaOH solution was removed
134 and the nanofiber residue was gently washed three times with
135 deionized water and once with acetone before finally dispersing
136 the fibers in decane (with sonication for ca. 2 s). Random arrays

of nanofibers were prepared by depositing 5 μL droplets of 137
fibers, suspended in decane, onto clean glass coverslips followed 138
by drying overnight in air. 139

Imaging and Optical Measurements. Scanning electron 140
microscopy (SEM) images were acquired using a field emission 141
instrument (FEI Quanta 3D DualBeam SEM, FEI) operating at 142
beam voltages of 1–10 kV. Atomic force microscopy (AFM) 143
images were acquired in tapping mode using a calibrated 144
instrument (Innova, Bruker AXS) with commercial tapping 145
mode probes (typical radius of curvature ca. 8 nm, front/side 146
cone angles of 15 ± 2°/17.5 ± 2° respectively and nominal 147
spring constant of 20–80 N/m; MPP-11123-10, Bruker AXS). 148
No processing was applied to data apart from background plane 149
subtraction. Luminescence microscopy images were acquired 150
using an upright epi-fluorescence microscope (BX51, Olympus) 151
equipped with a 100 W halogen lamp and a thermoelectrically 152
cooled color CCD camera (Fast1394 QICAM, QImaging). 153
UV–vis absorption spectra were acquired using a double-beam 154
spectrophotometer (V-650, Jasco) equipped with an optional 155
60 mm integrating sphere (ISV-722, Jasco). Photoluminescence 156
(PL) spectra were recorded using a luminescence spectrometer 157
equipped with a pulsed Xe short arc discharge lamp and 158
Czerny–Turner monochromators (QuantaMaster 40, Photon 159
Technology International). 160

PL Emission Quenching Studies. The emission quench- 161
ing response of PFO thin films and nanofiber arrays to vapors 162
of electron deficient analytes was ascertained by inserting one 163
such sample at a time into a sealed quartz cuvette containing 164
solid 2,4-DNT, DQ, or AQ at room temperature. The analyte 165
material had been presealed in the cuvette for 1 h in advance in 166
order to allow it reach its equilibrium vapor pressure. After a 167
certain time period had elapsed, the PFO sample was removed 168
from the cuvette and a PL spectrum was immediately recorded. 169
Thin film and nanofiber samples (on coverslips) were mounted 170
at 45° to the incident beam using a home-built coverslip holder 171
in a quartz cuvette that was placed into the cuvette holder of 172
the QuantaMaster 40 system. The solid quencher was placed at 173
the bottom of the cuvette to avoid direct contact with the 174
polymer sample on the coverslip. As a result, only vapors from 175
the analyte interacted with the PFO polymer sample. Single 176
nanofiber emission measurements were carried out using a 177
scanning confocal PL microscope (MicroTime 200, PicoQuant 178
GmbH) equipped with a 402 nm pulsed picosecond laser 179
diode. 180

181 ■ RESULTS AND DISCUSSION

Polyfluorene Nanofibers. PFO nanofibers were prepared 182
under ambient conditions via solution-assisted wetting of 183
porous anodized alumina membrane templates. Following 184
synthesis, the nanofiber-filled template was attached to an 185
adhesive carbon pad and the alumina host was selectively 186
dissolved in aqueous NaOH (3 M). The remaining nanofibers 187
were rinsed with deionized water and dried under nitrogen gas 188
flow. Scanning electron microscopy (SEM) images of a 189
freestanding PFO nanofiber array following selective removal 190
of the template are shown in Figure 1a and b. The data 191
demonstrate that close-packed forests of nanofibers were 192
formed (~10⁹ nanofibers/cm²). Statistical analysis of the 193
SEM image data indicated a mean nanofiber diameter of 208 194
± 30 nm, in good agreement with the nominal template pore 195
diameter; see Figure 1c. The fibers exhibited a smooth outer 196
surface morphology without obvious structural defects. 197

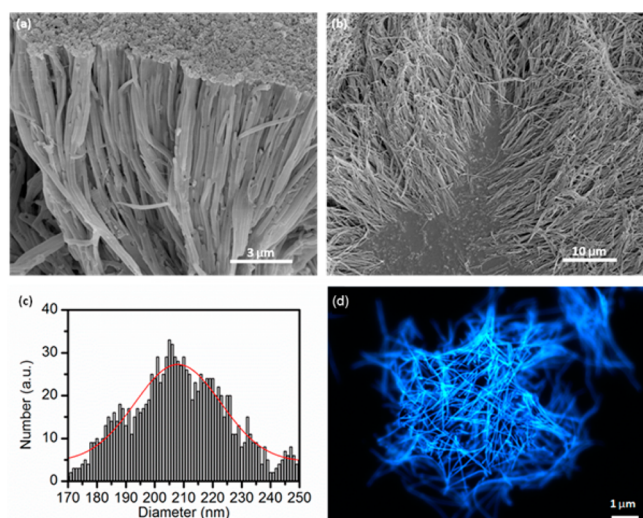


Figure 1. (a and b) Scanning electron microscopy images of a “forest” of nanofibers following selective dissolution of the alumina template. (c) Histogram of nanofiber diameters obtained following SEM image analysis. The solid red line is a Gaussian fit to the diameter distribution. (d) Epi-fluorescence image of a random PFO nanofiber array on a glass substrate.

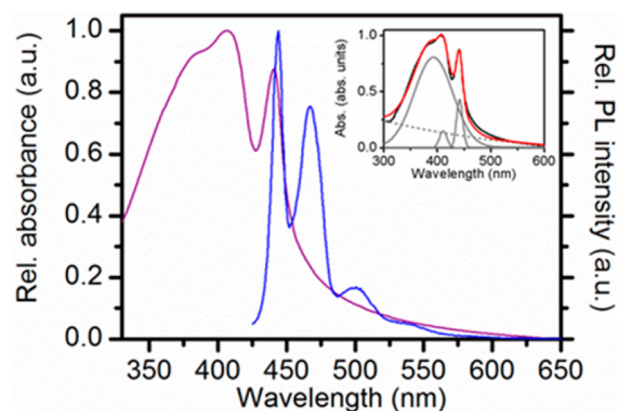


Figure 2. Intensity-normalized absorption (mauve line) and emission (blue line) spectra (λ_{ex} : 407 nm) of a random array of PFO nanofibers deposited on a glass substrate. (inset) Plot of three Gaussian functions (solid gray lines) and a background Gaussian function (dashed gray line) that were fitted to the nanofiber array absorption spectrum (solid black line). The sum of all four Gaussians is shown (red line).

198 An epi-fluorescence microscopy image of a dense array of
 199 nanofibers that was deposited onto a glass substrate from a
 200 decane suspension is shown in Figure 1d. Nanofiber length, L ,
 201 was found to range between 2 and 40 μm , and mean fiber
 202 length was found to be $15 \pm 2 \mu\text{m}$. Some degree of radial
 203 curvature was observed for the majority of the fibers, indicating
 204 the flexibility of these nanostructures. Uniform blue photo-
 205 luminescence with a low emission background was observed
 206 along the full lengths of the fibers, indicating that the nanofiber
 207 formation and extraction protocols provided dispersions of
 208 robust, discrete high-aspect ratio PFO nanofibers in a format
 209 suitable for deposition of nanofiber arrays. Additionally, the
 210 density of the deposited arrays could be readily tuned from
 211 dense, multilayer surface coverage to well-dispersed, submono-
 212 layer surface coverage by appropriate dilution of the nanofiber
 213 suspension.

214 Typical intensity-normalized absorption and PL spectra
 215 acquired for a random PFO nanofiber array on glass are
 216 shown in Figure 2. The absorption spectrum of the nanofiber
 217 array exhibited a band at ca. 395 nm (fwhm of ca. 110 nm) with
 218 a shoulder near 407 nm and a pronounced low energy peak at
 219 441 nm, the latter features being characteristic of the $S_0 \rightarrow S_1$
 220 0–1 and 0–0 transitions of β -phase PFO, respectively, and
 221 indicated that a fraction of β -phase chains had formed within
 222 the amorphous phase matrix of the PFO nanofibers.^{42,43} The
 223 long wavelength tail in this spectrum (above 450 nm) was
 224 attributed to a degree of optical scattering by the nanofiber
 225 array.⁴⁴ The PL spectrum of the nanofiber array exhibited
 226 comparatively narrow emission peaks (viz. the PL spectrum of
 227 an as-spun PFO thin film shown in Figure SI.1, Supporting
 228 Information) at 441, 467, and 500 nm, indicative of a narrowed
 229 distribution of emitting PFO chain segments with increased
 230 effective conjugation lengths. This spectrum was characteristic
 231 of the $S_1 \rightarrow S_0$ 0–0 transition, with associated vibronic replicas,
 232 of β -phase PFO.^{42,45}

233 The fraction of β -phase material present within the fibers was
 234 estimated by deconvoluting the absorption spectrum by fitting
 235 it with three Gaussian functions using a nonlinear least-squares

algorithm; see Figure 2, inset.⁴⁶ An additional Gaussian was fit
 236 to the data to account for the background signal, mainly due to
 237 optical scattering from the nanofiber array. The amount of β -
 238 phase was estimated by dividing the combined area of the
 239 Gaussians centered at 407 and 441 nm by the total area of all
 240 the fitted Gaussians (neglecting the contribution from the long
 241 wavelength tail). An upper limit value for the β -phase fraction
 242 of 7% was determined.⁴⁷

243 Overall, the spectroscopic data indicated that a fraction of the
 244 amorphous phase PFO molecules, with initially random
 245 molecular chain conformations, had adopted the more planar
 246 and extended 2_1 helical molecular conformation of the β -phase
 247 during synthesis;⁴⁸ see Scheme SI.3, Supporting Information.
 248 The nanofiber emission spectra were completely dominated by
 249 this fraction, due either to Förster-type energy transfer or to
 250 singlet exciton migration from the glassy phase to the lower
 251 energy β -phase.^{43,45,49} Formation of the β -phase within
 252 polymer fibers was attributed to the action of mechanical
 253 stresses that arose during solution-assisted filling of the alumina
 254 template pores and, afterward, during solvent evaporation.^{42,50}

255 **PL Quenching of Films and Nanofiber Arrays.** The
 256 photoluminescence behaviors of β -phase containing PFO thin
 257 films and nanofibers in the presence of vapors of an electron
 258 deficient analyte were compared by exposing individual samples
 259 to solid analyte material (that was presealed in cuvettes for 1 h
 260 in advance in order to allow the analyte reach its equilibrium
 261 vapor pressure) for specific periods of time prior to measuring
 262 PL spectra. PL spectra acquired for a typical, ca. 6.5 nm thick,
 263 β -phase containing PFO film on a glass substrate following
 264 exposure to DQ vapors for 0, 10, 30, 60, 120, 180, 300, and 600
 265 s, respectively, are shown in Figure 3a. For comparison, PL
 266 spectra acquired under identical conditions for a typical dense,
 267 random array of PFO nanofibers on a glass substrate are shown
 268 in Figure 3b. As expected, both film and nanofiber spectra were
 269 dominated by β -phase emission. Additionally, exposure to DQ
 270 vapors resulted in a marked and rapid quenching of both film
 271 and nanofiber emission. The time dependence of the quenching
 272 responses, determined by monitoring the intensity of the 0–1
 273 emission peaks (centered at 467 nm) as a function of exposure
 274 time indicated a decrease in film emission intensity of 73% after
 275 10 s, which progressed to 86% after 60 s. In contrast, nanofiber
 276 array emission responded more gradually during exposure to 277

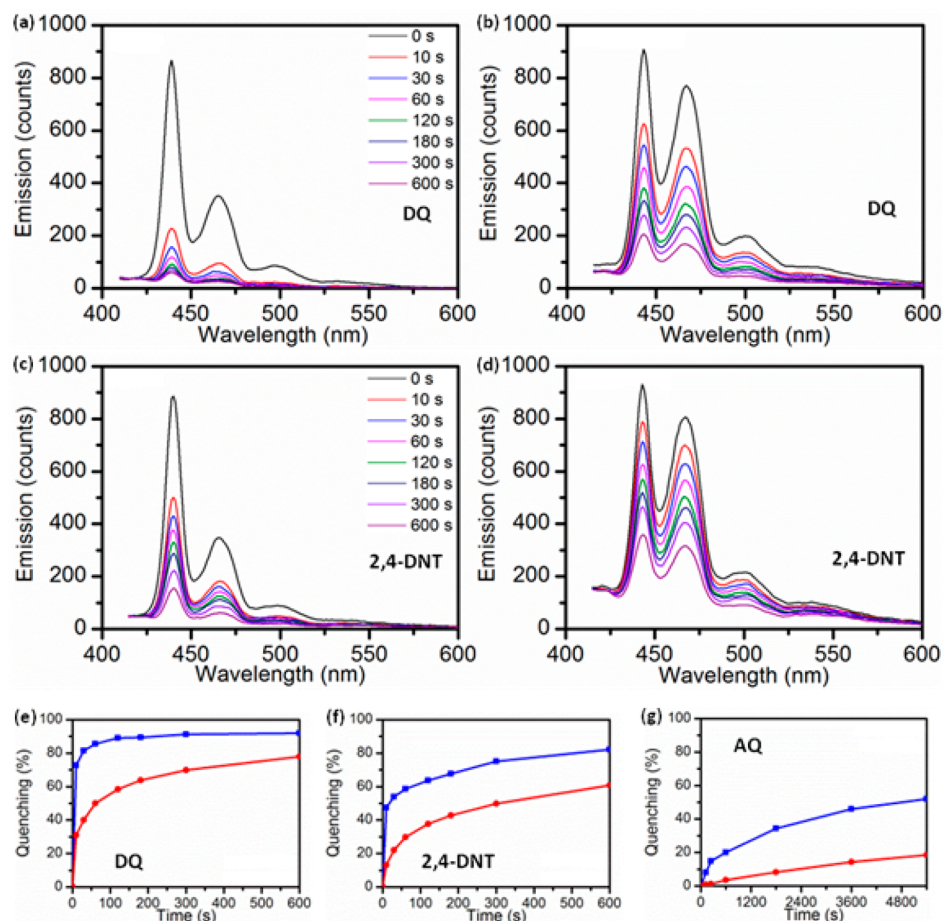


Figure 3. (a) PL spectra recorded for a typical β -phase containing PFO thin film on exposure to DQ vapor for different times. (b) Analogous data measured for a typical dense, random array of PFO nanofibers. (c) PL spectra recorded for a thin film on exposure to 2,4-DNT vapor for different times. (d) Analogous data measured for a dense nanofiber array. (e–g) Extent of PL quenching (decay of 0–1 peak intensity) for film (blue lines) and nanofiber array (red lines) samples as a function of exposure to DQ, 2,4-DNT, and AQ, respectively. Note: for all, $\lambda_{\text{ex}} = 401 \text{ nm}$.

278 DQ vapor, with a decrease in nanofiber emission intensity of
279 31% after 10 s, which progressed to 50% after 60 s; see Figure
280 3e.

281 PL spectra acquired for a typical β -phase containing PFO
282 film following exposure to 2,4-DNT vapors are shown in Figure
283 3c. For comparison, PL spectra acquired under identical
284 conditions for a typical dense, random array of PFO nanofibers
285 are shown in Figure 3d. Exposure to 2,4-DNT vapors resulted
286 in rapid emission quenching. The quenching responses
287 indicated a decrease in film emission intensity of 48% after
288 10 s, which progressed to 59% after 60 s. Again, nanofiber array
289 emission responded more gradually, with a decrease in fiber
290 emission intensity of 13% after 10 s, which progressed to 30%
291 after 60 s; see Figure 3f. Finally, the time dependent quenching
292 responses observed for a β -phase containing PFO film and a
293 dense, random array of PFO nanofibers following exposure to
294 AQ vapors are compared in Figure 3g. Exposure to AQ vapors
295 resulted in a notably slow quenching of emission. A decrease in
296 film emission intensity of 4% after 10 s, which progressed to 5%
297 after 60 s, was observed, while nanofiber emission intensity
298 decreased by 2% after 10 s and progressed to only 3% after 60 s.

299 **PL Quenching Mechanism and Trends.** Since the
300 wavelength range of the PFO emission was far above the
301 absorption range of the analytes (see Figure SI.5, Supporting
302 Information), emission quenching by excited state energy
303 transfer was considered unlikely. Therefore, the observed

quenching response was assigned to photoinduced electron 304
transfer from the excited PFO to the electron deficient analytes. 305
The overall free energy change, ΔG° , may be approximated by 306

$$\Delta G^\circ = E(P/P^{+\bullet}) - \Delta E_{0-0} - E(Q/Q^{+\bullet})$$

where $E(P/P^{+\bullet})$, ΔE_{0-0} , and $E(Q/Q^{+\bullet})$ are the oxidation 307
potential of the PFO polymer, the lowest singlet 0–0 excitation 308
energy of the polymer and the reduction potential of the 309
analyte, respectively.⁵¹ $E(P/P^{+\bullet})$ and ΔE_{0-0} values for glassy 310
phase PFO are 1.6 V (vs SCE)⁵² and 2.90 eV, respectively. 311
 $E(Q/Q^{+\bullet})$ values for 2,4-DNT, AQ, and DQ are –1.0, –0.9, 312
and –0.8 V (vs SCE), calculated from various different 313
electrochemical and optical measurement data; see Table 314
SI.1, Supporting Information.^{53–57} This results in ΔG° values 315
between –0.30 and –0.50 eV; see Scheme SI.4, Supporting 316
Information, for a schematic of the oxidative electron transfer 317
process. 318

The uptake, $M(t)$, of an analyte by a thin film over a given 319
exposure time period can be calculated by 320

$$M(t) = 2M(\infty) \sqrt{\frac{Dt}{\pi L^2}}$$

where D is the diffusion coefficient of the analyte within the 321
film, $M(\infty)$ is the mass uptake at the equilibrium point, taken 322
as SV where S is the solubility of the analyte within the film and 323

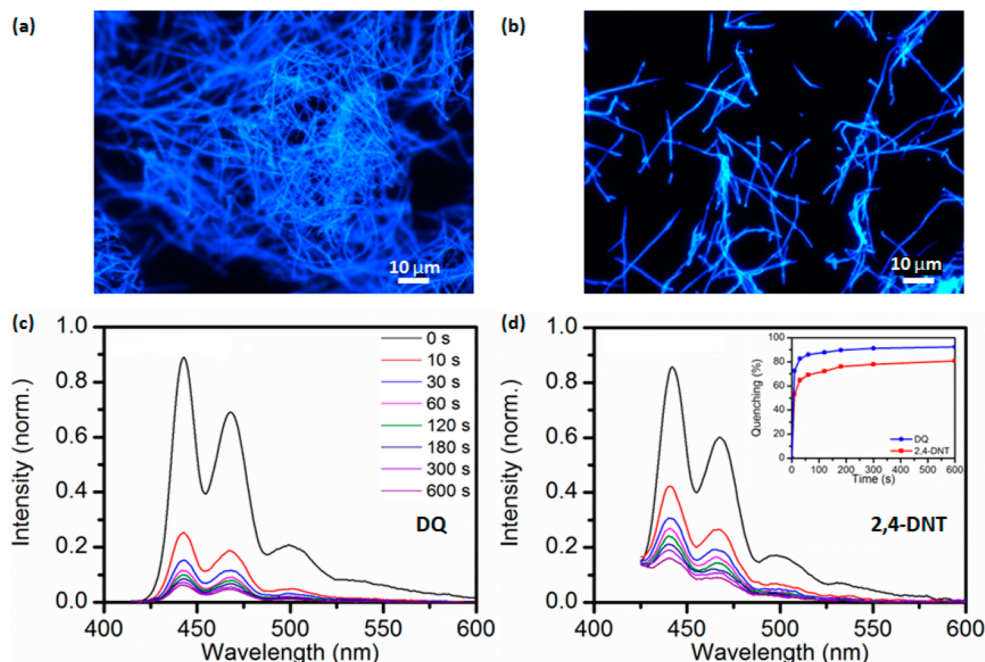


Figure 4. (a and b) Representative epi-fluorescence microscopy images of dense and disperse random nanofiber arrays, respectively. (c and d) Emission spectra (λ_{ex} : 401 nm) recorded for typical disperse nanofiber arrays on exposure to DQ and 2,4-DNT vapors, respectively, for different times. (inset) Extent of emission quenching (decay of 0–1 peak intensity) during exposure to DQ (blue) and 2,4-DNT (red), respectively.

324 V its volume, L is the film thickness (cm), and t is the total
325 exposure time.⁵⁸ To estimate the uptake of, e.g., 2,4-DNT by a
326 PFO thin film, mean values of D (1.1×10^{-9} cm²/s) and S (29
327 $\times 10^{-6}$ g/cm³) for 2,4-DNT were obtained for five different
328 polymers with comparable diffusivity and solubility to PFO.⁵⁹

329 Given that the PFO films were 2.42 cm² in area and 6.5 nm
330 in thickness, the total 2,4-DNT uptake after 18 s (ca. 50%
331 emission quenching) was estimated to be ca. 1.0×10^{-8} g or 5.9
332 $\times 10^{-11}$ mol. The total amount of PFO polymer within the film
333 was ca. 1.57×10^{-6} g (bulk PFO density of ca. 1 g cm⁻³
334 without compression)⁴³ giving a total number of 9,9-
335 dioctylfluorenyl monomers of ca. 5×10^{-9} M. Consequently,
336 the molar ratio of uptaken 2,4-DNT molecules to the total
337 number of available emissive fluorene monomers was about
338 1:85, indicating that emission quenching likely occurred via an
339 amplified luminescence quenching process mediated by PFO
340 polymer chains (which permitted exciton migration within the
341 film) rather than via direct quencher analyte–chromophore
342 interaction.⁶⁰ Since the film thickness was on the order of the
343 exciton migration range (0–5 nm) measured for amorphous
344 PFO,⁶⁰ this amplified quenching process facilitated effective
345 quenching of film emission with a 2,4-DNT exposure time of
346 only a few minutes.

347 While a strong, negative exergonicity (ΔG°) facilitates
348 emission quenching, the quenching rate (EQ) is also related
349 to the polymer–analyte binding strength (K_b) and the vapor
350 pressure of the quenching analyte molecules (VP) by the
351 expression $\text{EQ} \propto [\exp(-\Delta G^\circ)^2] K_b \text{VP}$.¹⁰ This is pertinent to
352 the present study since the quenching effectiveness of the
353 analytes above (DQ > 2,4-DNT > AQ) differed from the
354 relative magnitudes of the reaction exergonicities (DQ > AQ >
355 2,4-DNT); see Figure 3e–g. While it was not possible to obtain
356 exact values for the polymer–analyte binding constants (K_b),
357 polymer–analyte interactions may be considered in terms of the
358 free energy of mixing, i.e., $\Delta G_M = \Delta H_M - T\Delta S_M$.⁶¹ ΔH_M may
359 be estimated from $\Delta H_M = \Phi_A \Phi_P (\delta_A - \delta_P)^2$, where Φ_A and Φ_P

are the volume fractions of analyte and polymer, respectively,
360 and δ_A and δ_P are the corresponding solubility parameters.⁶¹
361 Since a negative ΔG_M is required for solubility, ΔH_M and ($\delta_A -$
362 δ_P)² (i.e., $\Delta\delta$) should be as small as possible. The Hansen
363 solubility parameters for PFO and the analytes⁶¹ were used to
364 estimate $\Delta\delta$ for each of the three polymer/analyte pairs; see
365 Tables SI.2 and SI.3 of the Supporting Information. 366

367 Qualitatively, for $\Delta\delta < 1$ analyte and polymer are expected to
368 be miscible, for $\Delta\delta = 1$ the components will be partially
369 miscible, and for $\Delta\delta > 1$ the components will become
370 progressively immiscible.⁶² Importantly, the order of the
371 magnitudes of the $\Delta\delta$ values estimated for each of the three
372 polymer/analyte pairs was consistent with their observed
373 quenching effectiveness. The role of the vapor pressure of the
374 analyte molecules (VP) in influencing EQ was also considered.
375 Again, the relative magnitudes of the equilibrium vapor
376 pressures were consistent with the observed order of quenching
377 effectiveness. The more effective PFO quenching response was
378 observed in the presence of DQ with a vapor pressure of DQ
379 (2.88×10^{-3} mm Hg, or 2324 ppb, at 25 °C), followed by 2,4-
380 DNT (1.47×10^{-4} mm Hg, or 118 ppb, at 25 °C) and AQ
381 (1.16×10^{-7} mm Hg, or 0.1 ppb, at 25 °C), respectively.⁶³

Role of Sample Morphology. From consideration of
382 Figures 3e–g, it is apparent that the EQ for each of the analytes
383 was greater for the ca. 6.5 nm thick β -phase containing PFO
384 thin films than for the PFO nanofiber arrays. Concerning the
385 morphology of the latter samples, dense nanofiber arrays were
386 typically observed to comprise multilayers of nanofibers
387 distributed in randomly stacked, disorganized arrangements;
388 see Figure 4a. To probe the effect of nanofiber density and
389 substrate surface coverage on the emission quenching response
390 of the arrays, lower density nanofiber arrays were prepared
391 using a diluted ($\times 4$) nanofiber/decane suspension; see Figure
392 4b. PL spectra acquired of disperse nanofiber arrays, comprised
393 of submonolayers of disperse, randomly distributed nanofibers
394 on glass substrates, following exposure to DQ or 2,4-DNT
395

396 vapors are shown in Figure 4c and d, respectively. Exposure to
 397 the DQ and 2,4-DNT vapors resulted in a prompt and
 398 significant quenching of nanofiber array emission. The time
 399 dependence of the quenching responses, determined by
 400 monitoring the intensity of the 0–1 emission peaks (at ca.
 401 467 nm) as a function of duration of exposure to DQ vapor,
 402 indicated a decrease in disperse nanofiber array emission
 403 intensity of 73% after 10 s, which progressed to 87% after 60 s;
 404 see Figure 4d, inset. While exposure to 2,4-DNT vapor resulted
 405 in slightly less pronounced emission quenching, the time-
 406 dependent quenching responses indicated a decrease in
 407 disperse nanofiber array emission intensity of 53% after 10 s,
 408 which progressed to 69% after 60 s. Therefore, the emission
 409 quenching responses of disperse PFO nanofiber arrays were
 410 markedly improved over the responses measured for dense
 411 nanofiber arrays and were very similar to those measured for β -
 412 phase containing PFO thin films; see Figure 3e and f.
 413 Specifically, the emission quenching responses to DQ vapor
 414 were practically identical for thin films and disperse fiber arrays
 415 (extent of array quenching at 60 s/extent of film quenching at
 416 60 s = 87%/86% = 1.01) while the responses measured during
 417 exposure to 2,4-DNT vapor were slightly more pronounced for
 418 nanofiber arrays than for thin films (extent of array quenching
 419 at 60 s/extent of film quenching at 60 s = 69%/59% = 1.17).

420 The observation that disperse arrays of ca. 200 nm diameter
 421 PFO nanofibers could act as luminescent reporters of the
 422 selected volatile electron deficient compounds and that, during
 423 exposure to these analyte vapors, they exhibited an emission
 424 quenching response which was comparable to that of the ca. 6.5
 425 nm thick PFO films (see Figure SI.5, Supporting Information),
 426 was very encouraging since the greater thickness of the fibers
 427 might have been expected to reduce their relative response. In
 428 this regard, assuming similar porosities and polymer–analyte
 429 interactions for the solution processed PFO films and
 430 nanofibers, a slower quenching response could be plausibly
 431 expected for the fibers as a result of the longer times that might
 432 be required for analyte molecules to diffuse into the interior of
 433 the material during the quenching process.

434 However, the improved emission quenching performance
 435 observed for the disperse nanofiber arrays suggested that
 436 geometric factors relating to the lower substrate coverage,
 437 providing a less crowded environment around each of the
 438 fibers, may play a role in the quenching response. Specifically,
 439 the cylindrical geometry of the disperse, randomly distributed
 440 fibers may offer a significant advantage over planar thin films for
 441 vapor detection, as sensor size and shape are known to deeply
 442 affect the time required to capture a given number of analyte
 443 molecules. For example, for a hemicylindrical sensor, it has
 444 been shown that the time required to accumulate analyte
 445 molecules on the sensor surface via static diffusion is
 446 significantly shorter than that required for a disk-shaped
 447 sensor.⁶⁴ Likewise, it has been predicted, and experimentally
 448 confirmed, that the response time for moisture diffusion *into* a
 449 cylindrical polymer sensor structure may be up to 10-fold
 450 shorter than that for a thin film sensor of identical thickness
 451 and composition.⁶⁵

452 Although a trade-off does exist between the average response
 453 time and minimum concentration of analyte molecules that is
 454 detectable by a sensor operating in a diffusion-limited regime, it
 455 has been shown that, for the same response times, the detection
 456 limit of a nanofiber sensor may still be 3–4 orders of magnitude
 457 higher than that of a planar sensor.⁶⁶ These observations justify
 458 the use of nanofibers in certain sensing applications and, for the

PFO nanofibers employed in this work, the geometric factors
 associated with the disperse nanofiber arrays likely facilitated
 access by the electron deficient quencher molecules to the
 excited states within the fibers enabling prompt quenching
 responses.

Single Nanofiber PL Quenching. Further studies were
 carried out on individual PFO nanofibers in order to explore
 the ultimate level of miniaturization attainable for this nanofiber
 based sensor format. To this end, single nanofiber optical
 measurements were undertaken using a time-resolved laser
 scanning confocal photoluminescence microscopy and spec-
 troscopy system; see Figure 5. In a typical experiment, a

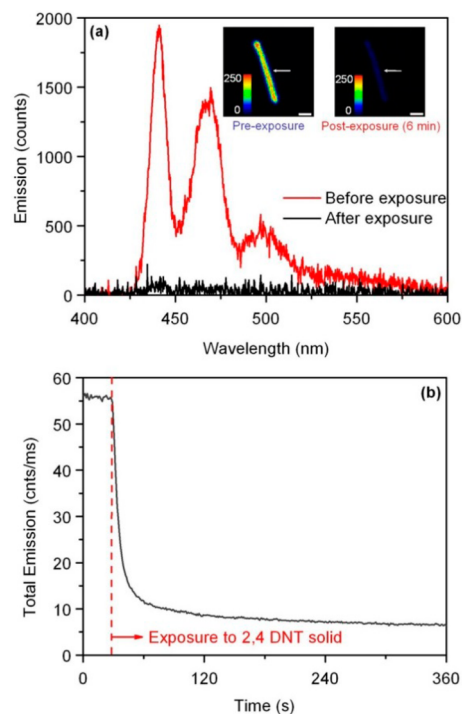


Figure 5. (a) PL spectra recorded for a single nanofiber before and after exposure to a nearby solid 2,4-DNT pellet. (inset) Scanning confocal emission intensity images of the fiber before and after exposure; arrows indicate the location at which data were acquired. (b) Emission intensity versus time trace measured for the nanofiber prior to and during exposure to the 2,4-DNT material. Note: for all, $\lambda_{\text{ex}} = 402$ nm.

scanning confocal emission intensity image and a location
 specific PL spectrum (λ_{ex} : 402 nm) were first recorded for a
 selected nanofiber on a glass substrate under ambient
 conditions. To prevent photobleaching, data were recorded
 quickly (images: 2 ms pixel integration time; spectra: 30 s
 integration time) at an incident excitation power <0.1 nW/cm².
 Then, to ensure that the nanowire emission output was stable,
 the integrated emission intensity ($\lambda > 430$ nm) was recorded in
 real time for 30 s at which point a solid pellet of 2,4-DNT
 material (51 mg) was gently placed into position at a height of
 5 mm above the nanofiber sample; see Scheme SI.2, Supporting
 Information. The nanofiber emission intensity was subse-
 quently recorded over a period of ca. 6 min. Following this, a
 second scanning confocal emission intensity image and
 spectrum were recorded for the fiber. Emission intensity
 images of a typical selected nanofiber that were recorded prior
 to and following exposure to 2,4-DNT in this manner are

488 shown in the inset to Figure 5. The nanofiber exhibited a 10-
489 fold decrease in emission intensity that was uniform along the
490 full length of the fiber, i.e., no residual emission “hot spots”
491 were observed. Corresponding PL spectra measured at a
492 location on the nanofiber before (black line) and after (red
493 line) exposure are shown in the main panel of Figure 5a.
494 Clearly, exposure resulted in an almost complete quenching of
495 the nanofiber emission. (Note that the apparent slight red shift
496 in the wavelength position of the 0–0 emission peak was an
497 artifact caused by the low transmission of the 430 nm long pass
498 filter.)

499 Finally, the emission intensity versus time trace was acquired
500 at the same location on the nanofiber; see Figure 5b. Prior to
501 placement of the 2,4-DNT material near the nanofiber, a stable
502 emission trace, with an average intensity of ca. 55 counts/ms,
503 was recorded. Immediately following placement, as 2,4-DNT
504 molecules volatilized from the surface of the solid sample,
505 entered the ambient atmosphere and diffused toward the
506 nanofiber, a dramatic decrease in nanofiber emission intensity
507 was observed. Under these conditions, the local concentration
508 of 2,4-DNT molecules in the vicinity of the nanofiber was
509 expected to be considerably less than that obtained using the
510 cuvette approach (i.e., equilibrium vapor pressure) employed
511 during the thin film and nanofiber array measurements
512 described above. Remarkably, for the single nanofiber, emission
513 was observed to rapidly drop by ca. 10% after only 1 s, by 50%
514 after 6 s, and by ca. 82% after 60 s. The good agreement
515 observed between data obtained during multiple measurements
516 at different locations along different fibers confirmed that the
517 reduction in nanofiber emission intensity were due to analyte-
518 induced emission quenching and not to localized photo-
519 bleaching. To estimate the vapor pressure of 2,4-DNT
520 molecules at the nanofiber surface, an approximation in terms
521 of diffusion from a planar surface using Fick’s law, made by
522 considering that the pellet dimensions were substantially
523 greater than those of the nanofiber, was used:

$$\frac{\partial \phi}{\partial t} = D \frac{\partial^2 \phi}{\partial x^2}$$

524 where D is the 2,4-DNT diffusivity in air ($0.203 \text{ cm}^2/\text{s}$)⁶⁷ and ϕ
525 is the flux of 2,4 DNT molecules. The resulting 1D solution is

$$\phi(x, t) = \phi(0, 0) \operatorname{erfc}\left(\frac{x}{2\sqrt{Dt}}\right)$$

526 Using this, and assuming that $\phi(0,0)$ is proportional to the
527 saturation vapor pressure of 2,4-DNT (140 ppb at $25 \text{ }^\circ\text{C}$),⁶³
528 the vapor pressure at the surface of the nanofiber array sample
529 1 s after placement of the pellet was estimated to be 25 ppb.
530 Assuming this represents the detection limit of the nanofiber
531 sensor, this compares very well with current commercially
532 available explosive sensors.^{18,19}

533 ■ CONCLUSION

534 The photoluminescence behavior of PFO nanofiber arrays
535 changes markedly in the presence of vapors of electron
536 deficient analytes, which cause significant quenching of
537 nanofiber emission via an amplified luminescence quenching
538 process. The observed order of analyte quenching effectiveness
539 is $\text{DQ} > 2,4\text{-DNT} > \text{AQ}$ indicating that, in addition to energetic
540 factors, analyte vapor pressure and polymer/analyte solubility
541 plays an important role in the emission quenching process.
542 Examination of the emission quenching responses of

submonolayers of disperse, randomly distributed nanofibers, 543
permits detection of nitroaromatics at subppm levels by 544
individual nanofibers. The observation that individual ca. 200 545
nm diameter PFO nanofibers exhibit an emission quenching 546
response competitive with that of ca. 6.5 nm thick PFO films, 547
suggests that geometric factors relating to the lower nanofiber 548
substrate coverage, providing a less crowded environment 549
around the fibers, combined with the nanocylindrical fiber 550
geometry, play a role in providing access by the electron 551
deficient quencher molecules to the excited states within the 552
fibers thereby facilitating the quenching response. 553

The results confirm that such nanostructures may success- 554
fully act as luminescent nanoscale vapor sensors and 555
demonstrate the performance that may be achieved by 556
controlling the structure and morphology of sensor transducer 557
elements at the nanoscale. Practical application of the PFO 558
nanofibers for volatile compound sensing requires a portable, 559
cost-effective device with full data connectivity for field 560
operations.⁶⁸ Ozcan and co-workers demonstrated fluorescent 561
imaging of single nanoparticles, viruses, and DNA fragments on 562
a smartphone-based optical reader,^{69,70} which was later used for 563
detection of parts-per-billion level detection of mercury 564
contamination in real world water samples.⁷¹ More recently, 565
Ming et al. reported the development of low-cost chip-based 566
wireless multiplex diagnostic device using a smartphone-based 567
optical reader.⁷² The excellent responsivity and signal-to-noise 568
ratios exhibited by the PFO nanofibers lend themselves to this 569
smartphone based approach for realization of an optical sensor 570
platform, with rapid response times and subparts-per-million 571
detection levels. 572

573 ■ ASSOCIATED CONTENT

574 ⓘ Supporting Information

Further experimental details. Characteristics of PFO thin films 575
and their luminescence responses to analytes. Key physical 576
parameters of the conjugated polymer/analyte system. 577
Comparative quenching responses of PFO thin films, nanofiber 578
arrays, and single nanofibers. This material is available free of 579
charge via the Internet at <http://pubs.acs.org>. 580

581 ■ AUTHOR INFORMATION

582 Corresponding Authors

*E-mail: hugh.doyle@tyndall.ie (H.D.). 583

*E-mail: gareth.redmond@ucd.ie (G.R.). 584

585 Notes

The authors declare no competing financial interest. 586

587 ■ REFERENCES

- (1) Janata, J. *Chem. Rev.* **2008**, *108*, 327–328. 588
- (2) Gardner, J. W.; Yinon, Y. In *NATO Science Series II: Mathematics, 589*
Physics and Chemistry; Kluwer Academic: Dordrecht, 2004. 590
- (3) Nagarajan, R.; Zukas, W.; Hatton, T. A.; Lee, S. *Nanoscience and 591*
Nanotechnology for Chemical and Biological Defense; ACS Symposium 592
Series; American Chemical Society: Washington, DC, 2009. 593
- (4) Senesac, L.; Thundat, T. G. *Mater. Today* **2008**, *11*, 28–36. 594
- (5) Moore, D. S. *Rev. Sci. Instrum.* **2004**, *75*, 2499–2512. 595
- (6) Meaney, M. S.; McGuffin, V. L. *Anal. Bioanal.Chem.* **2008**, *391*, 596
2557–2576. 597
- (7) Toal, S. J.; Trogler, W. C. *J. Mater. Chem.* **2006**, *16*, 2871–2883. 598
- (8) Germain, M. E.; Knapp, M. J. *Chem. Soc. Rev.* **2009**, *38*, 2543– 599
2555. 600
- (9) Tao, S. Y.; Yin, J. X.; Li, G. T. *J. Mater. Chem.* **2008**, *18*, 4872– 601
4878. 602

- 603 (10) Yang, J. S.; Swager, T. M. *J. Am. Chem. Soc.* **1998**, *120*, 11864–
604 11873.
- 605 (11) Le Barny, P. L.; Obert, E. T.; Soyer, F.; Malval, J. P.; Leray, L.;
606 Lemaître, N.; Pansu, R.; Simic, V.; Doyle, H.; Redmond, G.; Loiseaux,
607 B. *Proc. SPIE Int. Soc. Opt. Eng.* **2005**, 5990, 59900S.
- 608 (12) Bunte, G.; Hürtlen, J.; Pontius, H.; Hartlieb, K.; Krause, H.
609 *Anal. Chim. Acta* **2007**, *591*, 49–56.
- 610 (13) Germain, M. E.; Knapp, M. J. *J. Am. Chem. Soc.* **2008**, *130*,
611 5422–5423.
- 612 (14) Thomas, S. W.; Joly, G. D.; Swager, T. M. *Chem. Rev.* **2007**, *107*,
613 1339–1386.
- 614 (15) Östmark, H.; Wallin, S.; Ang, H. G. *Propellants Explos. Pyrotech.*
615 **2012**, *37*, 12–23.
- 616 (16) McQuade, D. T.; Pullen, A. E.; Swager, T. M. *Chem. Rev.* **2000**,
617 *100*, 2537–2574.
- 618 (17) Rochat, S.; Swager, T. M. *ACS Appl. Mater. Interfaces* **2013**, *5*,
619 4488–4502.
- 620 (18) Diehl, K. L.; Anslyn, E. V. *Chem. Soc. Rev.* **2013**, *42*, 8596–8611.
- 621 (19) FLIR Systems, L, pp FLIR Systems, Inc. Explosives & Narcotics
622 Detection. <http://www.flir.com/threatdetection> (accessed January 20,
623 2015).
- 624 (20) Zu, B.; Guo, Y.; Dou, X. *Nanoscale* **2013**, *5*, 10693–10701.
- 625 (21) Sirbuly, D. J.; Law, M.; Pauzaskie, P.; Yan, H. Q.; Maslov, A.
626 V.; Knutsen, K.; Ning, C. Z.; Saykally, R. J.; Yang, P. D. *Proc. Natl.*
627 *Acad. Sci. U.S.A.* **2005**, *102*, 7800–7805.
- 628 (22) Huang, J. X.; Virji, S.; Weiller, B. H.; Kaner, R. B. *J. Am. Chem.*
629 *Soc.* **2003**, *125*, 314–315.
- 630 (23) Naddo, T.; Che, Y. K.; Zhang, W.; Balakrishnan, K.; Yang, X.
631 M.; Yen, M.; Zhao, J. C.; Moore, J. S.; Zang, L. *J. Am. Chem. Soc.* **2007**,
632 *129*, 6978–6979.
- 633 (24) Che, Y. K.; Yang, X. M.; Loser, S.; Zang, L. *Nano Lett.* **2008**, *8*,
634 2219–2223.
- 635 (25) Zhao, Y. S.; Wu, J. S.; Huang, J. X. *J. Am. Chem. Soc.* **2009**, *131*,
636 3158–3159.
- 637 (26) Massuyeau, F.; Duval, J. L.; Athalin, H.; Lorcy, J. M.; Lefrant, S.;
638 Wéry, J.; Faulques, E. *Nanotechnology* **2009**, *20*, 155701.
- 639 (27) Fasano, V.; Polini, A.; Morello, G.; Moffa, M.; Camposeo, A.;
640 Pisignano, D. *Macromolecules* **2013**, *46*, S935–S942.
- 641 (28) Zang, L.; Che, Y. K.; Moore, J. S. *Acc. Chem. Res.* **2008**, *41*,
642 1596–1608.
- 643 (29) Zhao, Y. S.; Fu, H. B.; Peng, A. D.; Ma, Y.; Liao, Q.; Yao, J. N.
644 *Acc. Chem. Res.* **2010**, *43*, 409–418.
- 645 (30) Zhao, Y. S.; Peng, A. D.; Fu, H. B.; Ma, Y.; Yao, J. N. *Adv. Mater.*
646 **2008**, *20*, 1661–1665.
- 647 (31) McAlpine, M. C.; Ahmad, H.; Wang, D. W.; Heath, J. R. *Nat.*
648 *Mater.* **2007**, *6*, 379–384.
- 649 (32) Gu, F. X.; Zhang, L.; Yin, X. F.; Tong, L. M. *Nano Lett.* **2008**, *8*,
650 2757–2761.
- 651 (33) Pagliara, S.; Vitiello, M. S.; Camposeo, A.; Polini, A.; Cingolani,
652 R.; Scamarcio, G.; Pisignano, D. *J. Phys. Chem. C* **2011**, *115*, 20399–
653 20405.
- 654 (34) Cui, Q. H.; Zhao, Y. S.; Yao, J. *Chem. Sci.* **2014**, *5*, 52–57.
- 655 (35) Persano, L.; Camposeo, A.; Pisignano, D. *Prog. Polym. Sci.* **2014**,
656 DOI: 10.1016/j.progpolymsci.2014.1010.1001.
- 657 (36) Ramgir, N. S.; Yang, Y.; Zacharias, M. *Small* **2010**, *6*, 1705–
658 1722.
- 659 (37) Di Benedetto, F.; Camposeo, A.; Pagliara, S.; Mele, E.; Persano,
660 L.; Stabile, R.; Cingolani, R.; Pisignano, D. *Nat. Nanotechnol.* **2008**, *3*,
661 614–619.
- 662 (38) Huang, Y. W.; Quan, B. G.; Wei, Z. X.; Liu, G. T.; Sun, L. F. *J.*
663 *Phys. Chem. C* **2009**, *113*, 3929–3933.
- 664 (39) Garreau, A.; Massuyeau, F.; Cordier, S.; Molard, Y.; Gautron, E.;
665 Bertocini, P.; Faulques, E.; Wery, J.; Humbert, B.; Bulou, A.; Duval,
666 J.-L. *ACS Nano* **2013**, *7*, 2977–2987.
- 667 (40) Zhang, C.; Zhao, Y. S.; Yao, J. *New J. Chem.* **2011**, *35*, 973–978.
- 668 (41) Dawson, K.; Lovera, P.; Iacopino, D.; O’Riordan, A.; Redmond,
669 G. *J. Mater. Chem.* **2011**, *21*, 15995–16000.
- 670 (42) Grell, M.; Bradley, D. D. C.; Ungar, G.; Hill, J.; Whitehead, K. S.
671 *Macromolecules* **1999**, *32*, 5810–5817.
- (43) Ariu, M.; Lidzey, D. G.; Sims, M.; Cadby, A. J.; Lane, P. A.; 672
Bradley, D. D. C. *J. Phys.: Condens. Matter* **2002**, *14*, 9975. 673
- (44) Grell, M.; Bradley, D. D. C.; Long, X.; Chamberlain, T.; 674
Inbasekaran, M.; Woo, E. P.; Soliman, M. *Acta Polym.* **1998**, *49*, 439–
675 444. 676
- (45) Ariu, M.; Sims, M.; Rahn, M. D.; Hill, J.; Fox, A. M.; Lidzey, D. 677
G.; Oda, M.; Cabanillas-Gonzalez, J.; Bradley, D. D. C. *Phys. Rev. B* 678
2003, *67*, 195333. 679
- (46) Worsfold, O.; Hill, J.; Heriot, S. Y.; Fox, A. M.; Bradley, D. D. 680
C.; Richardson, T. H. *Mater. Sci. Eng., C* **2003**, *23*, 541–544. 681
- (47) Chunwaschirasiri, W.; Tanto, B.; Huber, D.; Winokur, M. *Phys.* 682
Rev. Lett. **2005**, *94*, 107402. 683
- (48) Lovera, P.; Redmond, G. *J. Nanosci. Nanotechnol.* **2013**, *13*, 684
5194–5202. 685
- (49) Khan, A.; Sreearunothai, P.; Herz, L.; Banach, M.; Köhler, A. 686
Phys. Rev. B **2004**, *69*, 085201. 687
- (50) Chen, S. H.; Su, A. C.; Chen, S. A. *J. Phys. Chem. B* **2005**, *109*, 688
10067–10072. 689
- (51) Chang, C. P.; Chao, C. Y.; Huang, J. H.; Li, A. K.; Hsu, C. S.; 690
Lin, M. S.; Hsieh, B. R.; Su, A. C. *Synth. Met.* **2004**, *144*, 297–301. 691
- (52) Janietz, S.; Bradley, D. D. C.; Grell, M.; Giebler, C.; 692
Inbasekaran, M.; Woo, E. P. *Appl. Phys. Lett.* **1998**, *73*, 2453–2455. 693
- (53) Chen, R.-F.; Zhu, R.; Fan, Q.-L.; Huang, W. *Org. Lett.* **2008**, *10*, 694
2913–2916. 695
- (54) Gong, X.; Moses, D.; Heeger, A. J.; Xiao, S. *Synth. Met.* **2004**, 696
141, 17–20. 697
- (55) Ma, W. L.; Iyer, P. K.; Gong, X.; Liu, B.; Moses, D.; Bazan, G. 698
C.; Heeger, A. J. *Adv. Mater.* **2005**, *17*, 274–277. 699
- (56) Liao, J.-L.; Chen, X.; Liu, C.-Y.; Chen, S.-A.; Su, C.-H.; Sut, A.- 700
C. *J. Phys. Chem. B* **2007**, *111*, 10379–10385. 701
- (57) Lu, H. H.; Liu, C. Y.; Chang, C. H.; Chen, S. A. *Adv. Mater.* 702
2007, *19*, 2574–2579. 703
- (58) Bai, H.; Shi, G. *Sensors* **2007**, *7*, 267–307. 704
- (59) Cragin, J. H.; Leggett, D. C. *Diffusion and Flux of Explosive-* 705
Related Compounds in Plastic Mine Surrogates; DTIC Document; 706
DARPA: Arlington, VA, 2003. 707
- (60) Stoessel, M.; Wittmann, G.; Staudigel, J.; Steuber, F.; Blassing, 708
J.; Roth, W.; Klausmann, H.; Rogler, W.; Simmerer, J.; Winnacker, A.; 709
Inbasekaran, M.; Woo, E. P. *J. Appl. Phys.* **2000**, *87*, 4467–4475. 710
- (61) van Krevelen, D. W.; te Nijenhuis, K. *Properties of Polymers*, 4th 711
ed.; Elsevier: Amsterdam, 2009. 712
- (62) Hansen, C. M. *Hansen Solubility Parameters: A User’s Handbook*; 713
CRC Press: Boca Raton, 2007. 714
- (63) *Handbook of Physical Properties of Organic Chemicals*; CRC 715
Press: Boca Raton, 1997. 716
- (64) Sheehan, P. E.; Whitman, L. J. *Nano Lett.* **2005**, *5*, 803–807. 717
- (65) Wegner, G. *Macromol. Chem. Phys.* **2003**, *204*, 347–357. 718
- (66) Nair, P. R.; Alam, M. A. *Appl. Phys. Lett.* **2006**, *88*, 233120. 719
- (67) Inglezakis, V. J.; Pouloupoulos, S. G. *Adsorption, Ion Exchange and* 720
Catalysis: Design of Operations and Environmental Applications; Elsevier 721
Science: Amsterdam, The Netherlands, 2006. 722
- (68) Walczak, R.; Dziuban, J.; Szczepańska, P.; Scholles, M.; Doyle, 723
H.; Krüger, J.; Ruano-Lopez, J. *Procedia Chem.* **2009**, *1*, 999–1002. 724
- (69) Wei, Q.; Qi, H.; Luo, W.; Tseng, D.; Ki, S. J.; Wan, Z.; Göröcs, 725
Z.; Bentolila, L. A.; Wu, T.-T.; Sun, R.; Ozcan, A. *ACS Nano* **2013**, *7*,
726 9147–9155. 727
- (70) Wei, Q.; Luo, W.; Chiang, S.; Kappel, T.; Mejia, C.; Tseng, D.; 728
Chan, R. Y. L.; Yan, E.; Qi, H.; Shabbir, F.; Ozkan, H.; Feng, S.; 729
Ozcan, A. *ACS Nano* **2014**, *8*, 12725–12733. 730
- (71) Wei, Q.; Nagi, R.; Sadeghi, K.; Feng, S.; Yan, E.; Ki, S. J.; Caire, 731
R.; Tseng, D.; Ozcan, A. *ACS Nano* **2014**, *8*, 1121–1129. 732
- (72) Ming, K.; Kim, J.; Biondi, M. J.; Syed, A.; Chen, K.; Lam, A.; 733
Ostrowski, M.; Rebbapragada, A.; Feld, J. J.; Chan, W. C. W. *ACS* 734
Nano **2015**, DOI: 10.1021/nn5072792. 735